Full-Duplex Underwater Acoustic Communications via Self-Interference Cancellation in Space

Yung-Ting Hsieh, Zhuoran Qi, and Dario Pompili

***Abstract*—Traditionally, underwater acoustic communications are half-duplex (HD), i.e., the hydrophones and transducers operate in non-overlapping time-slots/frequency-bands in one direction. To double the spectral efficiency into the full-duplex (FD) mode, which transmit and receive signals simultaneously, a self-interference cancellation (SIC) technique in space is introduced and deployed. Specifically, a novel underwater acoustic system is proposed to perform FD-SIC efficiently via an integrated design combining underwater acoustic vector sensor (AVS) and phased array transducer (PAT) to realize the spatial SIC. The energy focusing function of the beamformer (BF) helps PAT avoid self and mutual spatial interference. The AVS keeps updating the direction of arrival information to let BF adjust the steering angle via an adaptive protocol. The field-programmable gate array (FPGA) Direction of Arrival Estimation (DOA) estimation is done by a 12-element AVS, run-time is $1.22\times\mathbf{10}^{-4}$ s by MUSIC method, which is promising for real-time applications. In this work, phase-shift keying (PSK) and PSK-based orthogonal frequency-division multiplexing (OFDM) are deployed as the FD transmission modulation methods in the spacial SIC. The proposal is evaluated and verified via both simulations and emulations in real underwater acoustic channels collected in the Gulf of La Spezia, Italy, and it is able to achieve 59 dB SIC while modulating with binary phase-shift keying (BPSK) with carrier wave frequency 80 kHz and AVS steering angle $-5°$. Moreover, it has at least 37 dB SIC within the steering angle region.**

***Index Terms*—Acoustic vector sensors, full-duplex communications, interference cancellation, underwater acoustics.**

I. Introduction

BACKGROUND: In-band full-duplex (IBFD) communication techniques can potentially double the link capacity at the physical (PHY) layer and provide numerous benefits at higher layers by simultaneously transmitting and receiving on the same frequency band, which has been demonstrated to be feasible for wireless communications [2]. This technique can especially be beneficial for the current half-duplex (HD) underwater acoustic (UWA) communication systems since they suffer from low data rates and spectrum inefficiency. Given the slow propagation speed of acoustic waves compared to radio frequency (RF) propagation, while the distance between two sides of the link is extended by hundreds of meters, the defect of HD is considerably magnified. These reasons make the current techniques for full-duplex (FD) become indispensable for UWA applications.

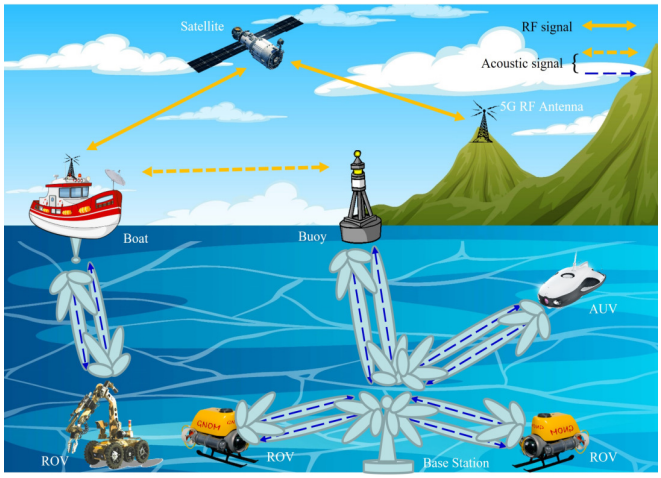

Fig. 1. Example of a FD communication with spatial SIC with various beamformed FD-PHY and MAC-based underwater acoustic signals.

Underwater sensor networks (UWSNs) are basically made up of a variety of sensors that communicate with various protocols in order to estimate underwater activities in various scenarios including different frequency carrier waves at different depths, temperatures, salinity and pH. Further than the PHY layer, the underwater devices such as autonomous underwater vehicles (AUVs), remotely operated vehicles (ROVs), etc., are working in a more complicated medium access control (MAC) layer. They exchange information with a centralized base station. The cross-layer architecture can be used to deploy various FD-based UWSNs in the river/ocean environment, as shown in Fig. 1. In the MAC layer, the cross-layer protocol architecture design allows underwater acoustic networks to be optimized. It eliminates the conventional constraint that information can only be transferred between two adjacent layers, while information can be exchanged between non-adjacent layers for the sake of reducing the complexity of the network and saving power. The PHY layer provides information about the estimated signal-to-noise ratio (SNR) as well as the frequency response to the MAC layer, which assists the MAC layer in resetting the back-off timer for re-transmissions, resulting in energy savings and reduced network end-to-end latency. As shown in Fig. 1, the UWSNs can work through terrestrial base stations, satellites, and floating buoys, using efficient energy utilization and joint optimization of their functionalities at different layers of the protocols stack. The cross-layer architecture can provide a roadmap to

Manuscript received April 18, 2022 revised October 10, 2022; approved for publication by Yik Chung Wu, Division 1 Editor, November 7, 2022.

Y.-T. Hsieh, Z. Qi, and D. Pomplili are with the Department of Electrical and Computer Engineering (ECE), Rutgers University–New Brunswick, NJ 08854, USA, emails: {yungting.hsieh, zhuoran.qi, pompili}@rutgers.edu.

A preliminary shorter version of this work appeared in the Proc. of *IEEE MASS*, Dec'20 [1].

This work was supported by NSF NeTS Award No. CNS-1763964.

Y.-T. Hsieh is the corresponding author.

Digital Object Identifier: 10.23919/JCN.2022.000052

1229-2370/23/$10.00

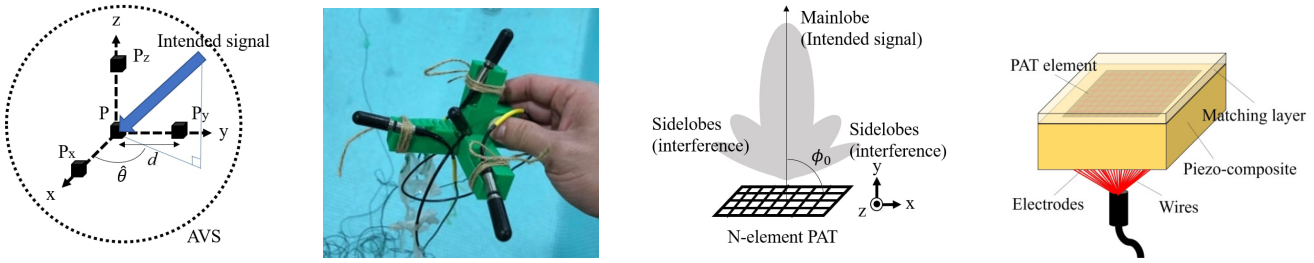

(a) (b) (c) (d)

Fig. 2. (a) 4-element acoustic vector sensor (AVS), where $\hat{\theta}$ is the estimated angle of direction on the x-y plane; (b) Photo of the proposed acoustic vector sensor, which is composed of 4 omni-directional hydrophones; (c) N-element uniform rectangular phased array BF, where ϕ_0 shows the steering angle; and (d) 3-D PAT sample image, in which each PAT element has an independent electrode at the bottom connected with a wire to the controller.

higher network throughputs. The described design focuses on energy efficiency, as energy consumption is a major concern in UWSNs, and underwater sensors are usually powered by batteries. When considering the centralized FD network structure in Fig. 1, the data link layer mainly considers the MAC layer algorithm and applies a cross-layer protocol architecture approach between the PHY layer and the MAC layer. Via channel information input from the PHY layer, the data link layer can distribute channel resources more effectively, resulting in increased channel resource usage and power savings. At the same time, the PHY layer boosts communication quality by responding to data link layer power adjustment and control signals. This cross-layer design reduces power consumption, defends against propagation delay, and increases throughput. However, the increase of the link number, especially the FD links, can generate significant self-interference (SI) in the MAC layer. Hence, the optimization of IBFD with PHY and MAC layers in a cross-layer perspective or an alternative way to avoid SI in the network is eagerly needed to be discovered in depth.

The main limitations of UWA FD communication systems includes the nonlinear distortion introduced by the power amplifier (PA) in the transmitter (Tx) chain, hydrophone pre-amplifier, transducers, and the destructive effect of the multipath, as well as the reflections caused by the UWA channel. Because of the high transmission power of the near-end transmission, a direct-path strong SI is usually observed, which can be a hundred dB higher than the noise floor in some communication scenarios. The conventional UWA FD self-interference cancellation (SIC) communications are usually compose of an analog SIC circuit and a digital SI canceller [3]. The analog SIC circuit in most situations are responsible for canceling direct path SI, nonlinear multipath SI, or nonlinear distortion caused by PA before low noise amplifier (LNA) and analog-to-digital converter (ADC). Digital SIC is placed after ADC to reduce the residual SI. Several algorithms in the literature are developed for enhancing the SIC capabilities at the digital canceller. While many algorithms investigate the digital SI cancellation to reduce residual SI after analog SIC circuits, few researches focus on improving analog SIC circuits or transducers. In order to bring about a new situation, recent researches focus more on the novel digital SIC methods or a new technique called spatial SIC. In the FD spatial SIC, the beamforming technique helps establish two directions in the link that avoid interfering with each other.

Motivation and vision: The main challenges that motivate us in this research include (i) Maximizing the link capacity; (ii) Minimizing the space on the AUVs and between the hydrophones while FD is in place; (iii) Saving the power/energy by presenting novel solutions and protocols; (iv) Improving the spectral efficiency in the narrow acoustic bandwidth. Most of the power-saving methods, which are introduced in the literature, are for external mechanics of the system. However, in this research, we provide an FD solution in space to save interior space by replacing analog circuit and digital SI canceller with a small and light power-saving field programmable gate array (FPGA) board that consumes only less than 2 W, therefore it can be easily mounted in the AUV. We apply underwater phased array transducers (PATs) to focus the data transmission in space as well as utilizing acoustic vector sensor (AVS) for receiving the directional beams and estimating direction of arrival (DoA), as shown in Fig. 2. The utilized power-saving FPGA board forms the beamform, calculates the steering angle in the space and encodes the data. Moreover, it estimates the DoA in the decoder on the other side of the link from the information by AVS and gyroscope. The proposed UWA spatial SIC system can be expanded to the networks with a large number of nodes as mentioned in the Sec. I, in which the nodes communicate with a central station, or have an ad-hoc topology as illustrated in Fig. 1. While the number of nodes in the network increases within the same bandwidth (BW), the benefits of our design are amplified more in view of the fact that our beamformed links are theoretically independent to minimize the interference with each other. To further improve the spectral efficiency, PSK-based orthogonal frequency-division multiplexing (OFDM) is also evaluated in our proposed FD communication system.

Our contribution: In this article, we propose a novel FD-UWA communication system structure where the Tx and receiver (Rx) are independently designed with a PAT and an AVS shown in Fig. 2. We present a new spatial SIC technique by setting up an appropriate phase delay to shape the beamforming pattern aiming at the Rx on the other side of the link to enhance the power efficiently in the desired direction and reduce the SI on the suppressed signal direction. We develop a 3-D AVS, which can be expanded from four to sixteen orthogonal arranged hydrophones. The new design is more affordable compared to expensive military AVS and more flexible in the space domain, as well as having a wide BW. To the best of our knowledge, this is the first study of

TABLE I
COMPARISON OF DIFFERENT FD SIC METHODS.

Type	Method	Key enhancements	Drawbacks	SIC	Simulator and/or testbed	Performance
RF	HTE 2017 [4]	(1) GD tap followed by HT; (2) Different I/Q scaling results in a time-domain-based EQ, hereby called HT Equalization (HTE).	SIC is nonuniform in the frequency spectrum.	Digital	Own computation framework, which is conducted on a PC.	Digital 23 dB
UWA	MLSC 2018 [3]	(1) Add sparse constraint to cost function of ML; (2) Use stochastic gradient of cost function iteratively to complete maximum likelihood estimation.	Cannot deal with high ISR condition with quantizing noise.	Analog + Digital	Own computation framework, which is conducted on a PC.	ML: 40 dB MLSC:43 dB (digital)
RF	BDoFS 2018 [5]	(1) An N-path-filter-based circulator-receiver FD beamforming at baseband with minimal overhead.	The transducer is space occupying and making unsymmetrical sidelobes. Exists Cross-Talk Self-Interference (CTSI) between every TX-RX pair.	Spatial + Digital	Own computation framework, which is conducted on a PC with own PCB circuit and chips.	Spatial 50 dB + Digital 30 dB
RF	FDE 2019 [6]	(1) Tunable, reconfigurable, high quality factor 2nd-order Bandpass Filters (BPFs) with FDE-based RF canceller; (2) Amplitude and phase controls to emulate the frequency selective antenna interface.	The SIC analog circuit board occupies the space, bandwidth might be limited.	Analog + Digital	NI USRP SDR.	Analog 52 dB + Digital 43 dB
UWA	RLS-DCD 2019 [7]	(1) Use the digitalized Power Amplifier (PA) output as the regressor to deal with the nonlinear distortions caused by the PA in the transmitted chain.	Only proposed in low frequencies with heavy instruments. Long convergence time make it hard to become a real-time FD.	Digital	Own computation framework, which is conducted on a PC with own instruments.	Digital 69 dB
UWA	This work 2020-2022	(1) The energy focusing function of the Beam-Former (BF) helps PAT avoid self and mutual spatial interference; (2) The AVS keeps updating the direction of arrival information to let BF adjust the steering angle via an adaptive protocol.	The grating lobe interference breaks the SIC when the position relative angle is below the threshold angle.	Spatial + Digital (digital is for DOA)	Own computation framework, which is conducted on a FPGA with own instruments.	Spatial 59 dB

FD SIC in such a structure via a system composed of both PAT and AVS [1]. The PAT transmits the beamformed data, and the AVS keeps tracking the angle of arrival in the space domain to achieve real-time FD-UWA communication, signal processed with powerful but power-saving FPGA. We are also the first to discuss the UWA spatial SIC and to investigate the relationship between steering angle and available BW for bandwidth-limited systems such as the underwater acoustic channel with phase-shift keying (PSK) and PSK-based OFDM modulations. The SIC ability in simulation and emulation based on real underwater acoustic channels collected in testbed experiments proves our method is an alternative to the analog SIC circuit. Moreover, performance of traditional PSK [8] and PSK-OFDM [9] is evaluated based on our proposed FD-UWA communication system. The results show that the PSK-OFDM further enhances spectral efficiency.

Article organization: The remainder of the article is organized as follows. In Sec. II, we review the state of the art in the field of study. In Sec. III, we introduce the proposed solution and the required mathematical framework. In Sec. IV, we present the simulations for our solution. Finally in Sec. V, we conclude the article and present future work.

II. RELATED WORKS

In this section, a review of the related work is presented. First, the state-of-the-art research in AVSs and BF is explained. Afterward, the related papers on FD-SIC and also space-domain RF SIC design are presented. Finally, related research on SIC design in underwater environments is described, and our contributions are highlighted against the other competing solutions, the comparison is shown in Table I.

AVSs and phased array BF: The application of AVS in the terrestrial scenarios is elaborated in [10]. It is shown that the AVS can be combined with L shaped or triangular located microphones. This approach is developed based on Khatri–Rao (KR) product by exploiting the subspace characteristics of the time-variant covariance matrices of the uncorrelated quasi-stationary source signals. Authors in [11] proposed an L-shaped AVS consisting of three microphones and investigated Bartlett beamforming (BB), Capons beamforming (CB), and eigenvector acoustic intensity vector for DoA estimation of a single source and multiple sources. AVS was also utilized in the underwater environment in our previous research [12], in which a new signal-space-frequency beamforming (SSFB) technique leverages an AVS and a beamformer for underwater video transmission. In [13], the authors implemented the AVS in OFDM underwater acoustic communication by combining pressure and velocity signals to get the spatial directivity and to enhance the SNR. It is shown that the bit error rate (BER) is reduced from 1.04% (only in pressure channels) to 0.02% (when it is combined with the velocity channel).

SIC in FD communications: Broadband FD in RF is a recent hot topic in both the industry and academia [4]. One of the challenges in FD SIC design is to achieve a wide bandwidth as well as to have a great performance in SI suppression. The research in this area usually deals with SIC circuits via several equalization taps. A recent work [4] focuses on emulating the group delay (GD) and complex impedance of the SI channel by proposing a SIC circuit that achieves 80 MHz of SIC BW using a single tap delay. The proposed method achieves 23 dB SIC at the center frequency and has good linearity, but it is not uniform in the frequency domain. Later a frequency-domain equalization method, which has a better selection capability in the frequency domain while using second-order bandpass filters (BPFs) [6] is proposed. However, the SIC analog circuit board occupies the space and needs an attenuator, a BPF, and a passband for each selected frequency interval. This approach might work well in RF to achieve broadband FD communications but is limited in UWA due to the restrictions of the BW. The potential candidate to realize

SIC in a massive multi-input multi-output (MIMO) system is artificial intelligence [14]. The authors propose an efficient SI channel estimation framework based on a partial training strategy for FD massive MIMO systems. In the proposed scheme, the pilot signals for SI channel training are allocated to a number of massive base station antennas to satisfy the limited training overhead constraint, and only a part of the SI channel vectors among the entire SI channel matrix corresponding to the allocated BS antennas is estimated for each transmission block. A Doppler radar-based FD communication has been introduced in [15], in which an electrical balance duplexer (EBD) suppresses the direct SI so as to allow receiving the required environmental reflection for the Doppler measurement.

Space-domain RF SIC design: An FD circulator-receiver phased array, which employs SIC via beamforming, is presented in [5]. Fewer elements of the phased array widen the mainlobe and sidelobes, which results in a worse selectivity in space and also causes asymmetry in the beamforming pattern. Moreover, the individual channels make the SIC board space-occupying. Afterward, the wideband FD phased array with joint transmit and receive beamforming, presented in [16], extends the applications in space. While the power is concentrated, the SI channels are magnified to N^4, where N stands for the number of elements in the phased array, caused by setting the phased array antenna at both Tx and Rx. The beamforming method has also been presented to help real-time communication in the MIMO UAVs network for unknown input observer approach [17]. The proposed spatial estimation algorithm relies on using a delay-tolerant observer-based predictor, which can accurately predict the positions of the target UAVs in the presence of uncertainties due to factors such as wind gusts. The solution, which uses discrete-time unknown input observers, reduces the joint target detection and communication complication notably by operating on the same device and performs reliably in the presence of channel blockage and interference.

UWA SIC design: An SI channel estimation algorithm based on a maximum-likelihood estimator in IBFD underwater acoustic communication system [3] is designed to give better channel estimates in the presence of the non-Gaussian noise. When the interference to signal ratio (ISR), in which ISR stands for the SI power to intended signal power ratio at the input of digital SI cancellation, is too high, the digital SIC cannot compensate and decode the signal. For this issue, our proposed method in this article is the key to avoiding the high ISR condition. The low-complexity recursive least-squares (RLS) adaptive filter with dichotomous coordinate descent iterations is presented in [7] for nonlinear distortions caused by the PA in the transmitter chain. The experiment is transmitted in BPSK symbols at a carrier frequency f_c of 12 kHz with heavy instruments. The power spectra of the received signal before and after the digital cancellation shows a smooth pattern in frequency domain at the PA output. However, this method needs around 2 s for convergence, which makes it an impractical solution for FD communications. An adaptive technique to equalize the nonlinear distortion, introduced by the pre-amplifier, is proposed in [18]. The equalization is performed in the passband to avoid additional distortions due to the passband to baseband conversion. In [19], the reflections are also considered in the SI, and the received signal is taken as the superposition of reflections from the sea surface and seafloor with different arrival time. In [20], a variable BW from 30 kHz to 180 kHz is considered, and the relationship between coherent-to-incoherent Intensity Ratio (CTIR) and arrival time, channel variation ratio (CVR), and frequency are presented for solving reflection-based SI.

Underwater wireless communications: Passive time reversal (PTR) communication techniques for multipath interference in shallow sea acoustic channels are quantitatively evaluated by applying a PTR-decision feed-back filter (DFF) scheme in [21]. However, it is found that PTR has a performance limitation, which is output SNR (OSNR) converging to a typical value depending on the number of receivers. OFDM is one of the main streams of underwater wireless communications since it has advantages of (i) High spectral efficiency; (ii) Robustness against the frequency selective fading channel; (iii) Eliminating inter-symbol interference (ISI) by introducing cyclic prefix (CP). Authors in [22] study the effect of acoustic-shell coupling on near-end SI signal of IBFD UWA communications with OFDM. In [23], the SI channel impulse response is characterized with OFDM signals. In [24], authors propose a closed-form expression of the Doppler power spectrum model for UWA channels. The Doppler power spectrum can be modeled as a summation of the Spike shape and the Gaussian shape. The Spike shape presents the Doppler component from the Tx/Rx movement, while the Gaussian shape presents the Doppler component from the sea-surface motion. In [25], authors study the use of adaptive orthogonal frequency division multiple access (OFDMA) in a downlink scenario, where a central node sends data to multiple distributed nodes simultaneously. They explore the CSI feedback for resource allocation. An adaptive power-bit loading algorithm is presented, which assigns subcarriers to different users and allocates power and bits to each subcarrier, aiming to minimize the BER under power and throughput constraints. In [26], we propose an OFDM-based pulse position modulation (PPM), which improves the coverage distance significantly in underwater wireless optical communications. In [9], [27], and [28], we study the PSK-OFDM-MIMO for multimedia transmissions in the UWA communication. The results show the reliability of OFDM in the narrow bandwidth of the UWA communication systems. To defend against multipath effects and additive noise in UWA communications, we derive the circular time shift modulation (CTSM) in [29]. To realize a efficient and robust UWA communication system, we propose the spatial-modulation-based orthogonal signal division multiplexing (SM-OSDM) in [30]. In [31], we propose a machine-learning-based Doppler tracking and compensation method. In this work, we present the performance of traditional PSK and PSK-OFDM based on our proposed FD SIC system.

III. Proposed Solution

To establish the spatial SIC system, we introduce the mathematical backgrounds of AVS for the DoA estimation, including direct measurement, BB and CB methods with different number of elements in the AVS, structure and parameters of

PAT for focusing as well as steering the transmitted signal in Sec. III-A. In Sec. III-B, we elaborate on the framework of the hybrid system, which utilizes AVS and PAT as Tx and Rx by taking advantages form both of them to establish a beamforming-based FD SIC in the space domain. The goal of our spatial SIC design is to substitute the analog SIC circuit before the LNA with a new design proposed in this article. Three main benefits of our design include (i) Saving the space of analog SIC circuit; (ii) Limiting the transmitting angle to avoid nonlinear SI caused by multipath or by PA via its circuit; and (iii) Updating the DoA information to the other side of the link as a feasible solution for underwater applications while the vehicles, ships or buoys are floating in the water. In this article, we mainly focus on a 3-D solution and adjust the horizontal steering angle to demonstrate our design.

A. AVS and PAT, the Tx and Rx in the FD system

A vector sensor is a device that can measure the relationship between pressure channels and particle velocities [32]. The velocity channel in the x, y, and z directions are defined as,

$$v_x = -\frac{1}{j\rho_0\omega_0}\frac{\partial p}{\partial x}, \quad v_y = -\frac{1}{j\rho_0\omega_0}\frac{\partial p}{\partial y}, \quad v_z = -\frac{1}{j\rho_0\omega_0}\frac{\partial p}{\partial z}, \tag{1}$$

where p is the sound pressure at the origin, j is the unit imaginary number, ρ_0 is the density of the fluid, and ω_0 shows the angular frequency of the transmitted signals. An acoustic vector sensor can be imagined as three directional vector sensors (particle velocity meter) with an omni-directional pressure meter [33]. The particle velocity is used in the process of DoA estimation. Apart from directly measuring the particle velocity, which is called P-U method and P-P method, which only measures pressure is more commercially practical. The P-P method is based on the estimation of pressure gradient by setting closely located pressure sensors [34]. The AVS we propose in this research takes advantage of P-P method with structure in Fig. 2(a) and realized via 3D-printed structure as Fig. 2(b). In Fig. 2(b), a series of highly sensitive hydrophones, called RESON TC 4013 [35], are deployed. Distances between hydrophone on the origin and on the x-axis, y-axis, and z-axis are 8 cm. The DoA estimation from AVS is achieved with the acoustic intensity method. The acoustic intensity is the amount of acoustic energy flow in a certain angle interval and can be expressed as the product of particle velocity v and scalar pressure p at a point location r,

$$I(r,t) = p(t)v(r,t). \tag{2}$$

Here, $\hat{I_x}$ stands for the average acoustic intensity measured from two omni-directional sensors along with x-axis. The time dependent scalar pressure $p_{00}(t)$ and $p_{d0}(t)$ represent the pressure at origin and coordinate (d, 0, 0), respectively.

$$\hat{I_x} = -\frac{1}{\rho_0 d}\int_{-\infty}^{\infty}\frac{1}{\omega}\Im[\Gamma_{p_{00}p_{d0}}(\omega)]dw \tag{3}$$

Similarly, $p_{00}(t)$ and $p_{0d}(t)$ represent the pressure measured at origin and coordinate (0, d, 0), respectively. The intensity along y-axis is given by,

$$\hat{I_y} = -\frac{1}{\rho_0 d}\int_{-\infty}^{\infty}\frac{1}{\omega}\Im[\Gamma_{p_{00}p_{0d}}(\omega)]dw. \tag{4}$$

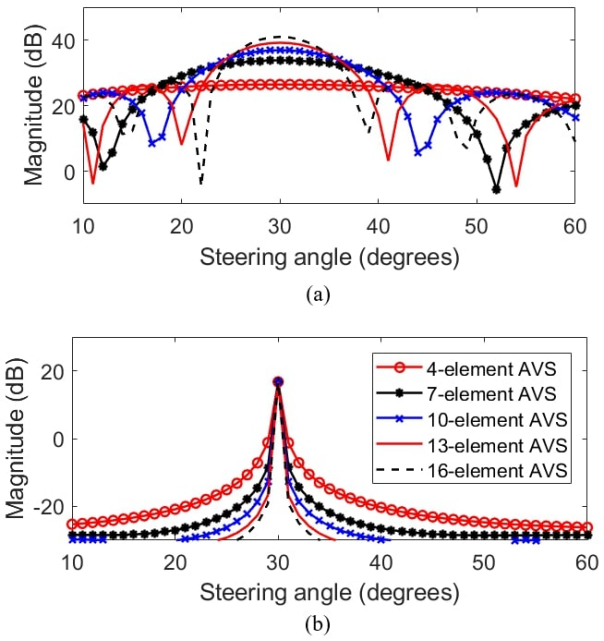

Fig. 3. Direction of arrival estimation via AVS with (a) BB; and (b) CB methods via 4-element AVS, 7-element AVS, 10-element AVS, 13-element AVS and 16-element AVS. The signal is designed from 30° on the x-y plane.

While considering the horizontal plane, by gathering scalar and pressure information from the AVS, the estimated DoA from the AVS is given by,

$$\hat{\theta} = \arctan\left(\frac{\hat{I_y}}{\hat{I_x}}\right). \tag{5}$$

Apart from the sound intensity method, the AVS can also serve as a spatial filter. Two DoA estimation methods using maximum power output (w) called Bartlett beamformer (BB) and Capon beamformer (CB) are given by,

$$w_{BB}(\theta) = \begin{bmatrix} 1 \\ \sin\theta \\ \cos\theta \end{bmatrix}^T [R_u] \begin{bmatrix} 1 \\ \sin\theta \\ \cos\theta \end{bmatrix}, \tag{6}$$

$$w_{CB}(\theta) = [w_{BB}(\theta)]^{-1}. \tag{7}$$

R_u is the largest eigenvector that points to the direction of the sound source. The signal source is designed on 30°. As shown in Fig. 3(a), while putting more elements in the AVS–i.e., one at the origin and two arranged on the x-axis, y-axis, and z-axis for a 7-element AVS–the DoA estimation that comes from BB can be improved. On the other hand, the CB method in Fig. 3(b) is computationally intensive due to the inverse of the covariance matrix, but is more precise even with few elements in AVS.

The PAT is introduced as a bandpass filter in the space since we majorly take its beamforming capability to focus the energy in certain directions for the intended signal. This kind of transducer is made of piezoelectric ceramics in Fig. 2(d). After polarization, the piezoelectric ceramics would have displacement in polarized directions once applied an alternating current (AC) voltage signal. We consider an available model specification from Callaghan Innovation, New Zealand. The

side length of the piezoelectric ceramics bulk is 103 mm, and the bulk is sliced into 144 (12×12) elements. The distance d between each center of element is 8.58 mm, as we consider the sound speed of water is 1500 m/s, the ratio of d over λ is 0.57 at center frequency 100 kHz. Each element is attached by wires then the beamforming pattern could be arranged by choosing different sections of elements from the matrix. Between the piezoelectric ceramics and water is a soft matching layer, it can help to reduce the difference in acoustic impedance between piezoelectric ceramics and water to prevent energy loss.

Massive beamforming theory including beam shape, directivity and aperture are elaborated in [36]. In our spatial SIC, we not only wish to create a narrow beam in space but wish to *electronically* rotate the mainlobe of the beamforming pattern from PAT in Fig. 2(b). The PAT steers in a certain direction, which is aiming at the other system, the array pattern towards a certain direction, say ϕ_0 (marked in Fig. 2(b)), without physically rotating it. The corresponding wavenumber at the desired look-direction is,

$$\psi_0 = kd\cos\phi_0. \tag{8}$$

Such steering operation can be achieved by wavenumber translation in ψ-space, that is, replacing the broadside pattern $A(\psi)$ by the translated pattern $A(\psi-\psi_0)$. Thus, we define $A'(\psi) = A(\psi-\psi_0)$ and the steered wavenumber as,

$$\psi' = \psi - \psi_0 = kd(\cos\phi - \cos\phi_0). \tag{9}$$

The maximum of $A'(\psi)$ will coincide with the maximum of $A(\psi')$, which occurs at $\psi' = 0$, or equivalently at $\psi = \psi_0$, or at angle $\phi = \phi_0$. It follows from the translation theorem of Fourier transforms that the weight coefficients $a_n{}'$ of the translated pattern $A'(\psi)$ will be given by $a_n{}' = a_n e^{-j\psi_0 n}$. We have,

$$\begin{aligned} A'(\psi) &= \sum_n a_n{}' e^{-j\psi n} = \sum_n a_n e^{-j(\psi-\psi_0)n} \\ &= \sum_n a_n e^{-j\psi' n} = A(\psi'). \end{aligned} \tag{10}$$

Because of the progressive phase factors $e^{-j\psi_0 n}$ in the weights $a_n{}'$, the steered or scanned array is sometimes called a phased or scanning array. The concepts of visible region, beamwidth, and the condition for absence of grating lobes, translate with minor modifications to the case of a steered array. As the angle ϕ varies over $0°\leqslant\phi\leqslant 180°$, the translated wavenumber ψ' in (9) varies over the shifted visible region,

$$-kd(1+\cos\phi_0)\leqslant\psi\leqslant kd(1-\cos\phi_0). \tag{11}$$

To ensure there are no grating lobes, ψ' must remain strictly less than 2π, which results in the sufficient condition, $kd(1+|\cos\phi_0|) < 2\pi$, or replacing $kd = 2\pi d/\lambda$, we get the most important equation to avoid SI in space, i.e.,

$$d < \frac{\lambda}{1+|\cos\phi_0|}. \tag{12}$$

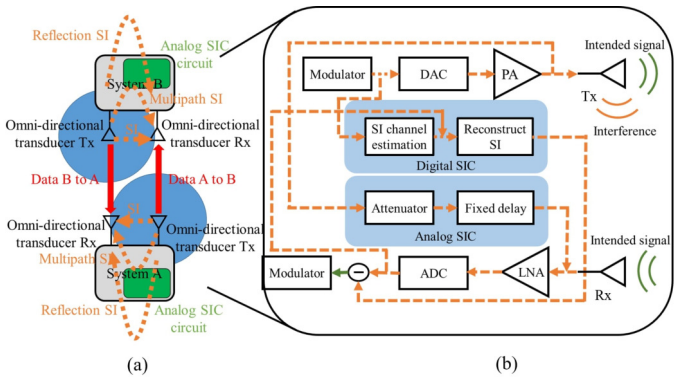

Fig. 4. (a) Conventional technique with analog SIC circuit; and (b) The block diagram of conventional UWA FD SIC communication system (green solid line: intended signal, orange dash line: interfered signal).

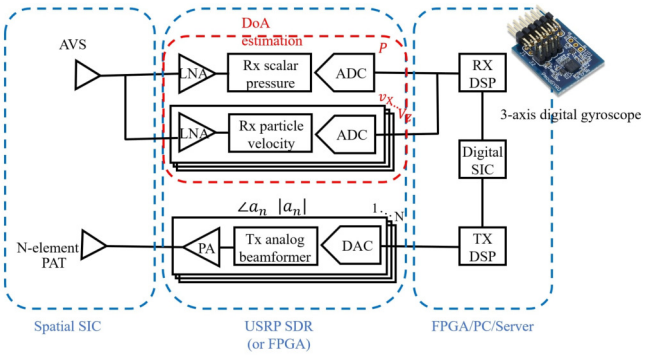

Fig. 5. Block diagram of FD-UWA spatial SIC with AVS and PAT system, the DoA method in the figure is the acoustic intensity method (labeled red), can be replaced by other DoA estimation methods like BB, CB, or multiple signal classification (MUSIC).

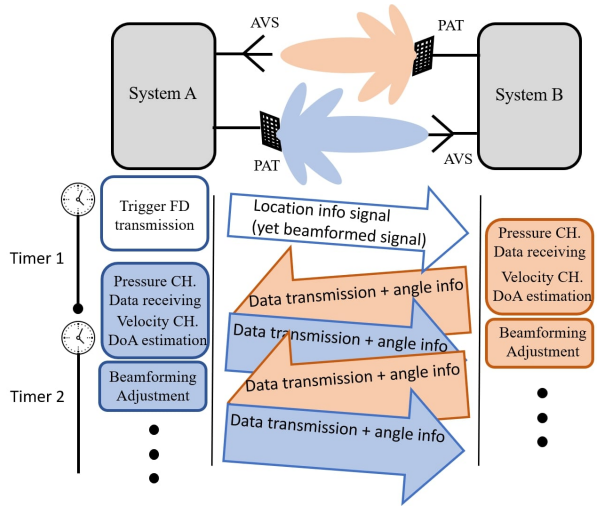

Fig. 6. Protocol of the UWA FD spatial SIC with AVS and PAT system. The time sequence of System A and B ensures Spatial SIC follows the sequence: Getting information, confirmation, then data transmission.

B. Hybrid System in Full-duplex Wireless Transmission

Fig. 4 shows the conventional technique with an analog SIC circuit to avoid SI from omni-directional transducers. In our research, we take advantage of AVS and PAT, combining them together (Fig. 5) to replace omni-directional transducer, which

is generally utilized in this field. The USRP SDR (or FPGA) at the receiver side needs four channels to catch pressure from each element on the AVS for conducting acoustic intensity method DoA estimation. Otherwise takes beamforming methods like BB, CB, or MUSIC to estimate the direction of signal arrival. While choosing BF to send out data, we set the beamforming pattern aiming at the other system's receiver, which is shown in Fig. 6. In this way, the receiver at the same side only receives the sidelobe suppressed signal to avoid the interference, which is usually done by the analog SIC circuit. Besides, our independent design of transmitter and receiver also prevents the receiver from receiving the reflected signal, which appears if using the transceiver's circulator.

Imagine we have system A and system B as shown in Fig. 6, while system A is receiving signals via AVS, it gets not only data from sound pressure but also particle velocity to realize the direction that the signal comes from. Then the direction of arrival estimation information can be added to the signal, which will be transmitted at the next time slot. Later, system B receives the data (from pressure) and the angle information (also from pressure). In this structure of dual-directional data transmission, the interference signal can be blocked and either system A or B continuously knows the angle between each other. If their relative location is moving, each system has enough information to adjust the beamforming steering angle. It is worth noting that a Pmod GYRO [37], stands for 3-axis digital gyroscope. The gyroscope inserted on the FPGA board gives the absolute angle information and the AVS provides the relative angle information to the hybrid system. This gyroscope consists of a low-power three-axis angular rate sensor L3G4200D, which has a sensitivity up to $70\ \mathrm{mdps/digit}$ while the full scale range FS = 2000 degrees per second (dps). Moreover, the gyroscope can update the angular information up to 800 times per second, which provides sufficient information to let the system achieve a real-time spatial SIC.

We develop an adaptive algorithm for our spatial SIC in the FD-UWA system as shown in Algorithm 1 for floating/moving devices like ROV, AUV, buoy, etc., and a fixed device like the centralized base station. In Algorithm 1, the inputs are the pressure signals from 4-elements AVS, whereas the outputs are the DoA angle $\hat{\theta}$ and the intended data. Assume system A initiates the procedure. After the spatial SIC is triggered, it starts getting absolute angle information from the gyroscope and sending it out. In the meanwhile, once the Rx on system A receives the signal from system B, system A calculates the DoA combined with the absolute angle from system A and B to form the steering data signal. If the DoA is out of the steering angle region judged by line 5, it sends back spatial SIC invalid and asks the underwater robot/vehicle to rotate the PAT. To detect whether the DoA is out of the valid region, the simplest method is a threshold-based detection. However, due to the underwater environment being filled with noise and reflections to affect DoA estimation, an artificial intelligence anomaly detection [38, 39] is prospective to have better performance in making sure the spatial SIC is set in proper condition. Data is the intended signal that can be modulated via a binary PSK (BPSK), quadrature PSK (QPSK), 8-quadrature amplitude modulation (QAM), and 16-QAM,

Algorithm 1: Framework for FD System A

```
   Input: Input parameters p, p_x, p_y, p_z
   Output: Output results θ̂, data_{b→a}
1  while operating spatial SIC do
2      Send(position, pilot) non-directionally;
3      if triggered by received signal then
4          Run DoA estimation to get θ̂ (AI, BB, CB,
           MUSIC) and channel estimation;
5          if θ̂ is out of steering angle region then
6              Report spatial SIC is invalid;
7              Ask underwater robot/vehicle rotate body
               or rotate PAT
8          else
9              Classify the optimized modulation and
               bandwidth;
10             Adjust steering angle ψ_0;
11             Simultaneously AVS receive data_{b→a} and
               send data_{a→b};
12             if triggered by another received signal then
13                 Boot up the another spatial SIC system
                   and run Algorithm 1 on the system
14             end
15         end
16     end
17 end
```

with the BW corresponding to the steering angle region. When system A receives the signal, it extracts the data to demodulate. System B is a mirror image symmetry of system A. System A and B will achieve a stable status transmitting data and angle information as shown in line 11. In case the relative location of systems A and B changes too much, which causes signal loss, they get reset to send the absolute angle information. For Algorithm 1, if the system A is considered as a fixed position station. It does not need a gyroscope to acquire the absolute angle from gravity. As an alternative, it must send out its location information; hence the other end of the link can aim the steering angle at the station and understand the role itself in the MAC layer. In the scenario of being triggered by the signal coming from another angle, the station will arrange another spatial SIC system to conduct another FD link, which is shown in line 12. For the floating systems like ROV, AUV, buoy, etc., this function is optional.

To evaluate and optimize the performance of our spatial SIC in the FD system in every modulation and bandwidth, we firstly adopt BPSK modulation to transmit a randomly generated signal. BPSK modulates the baseband signal into the central frequency of our transducers in the system with two phases. For example, mapping randomly generated 0 and 1 series data into a $100\ \mathrm{kHz}$ carrier wave on the complex plane corresponding to -1 and 1, which has a 180-degree phase in difference. A BPSK modulated signal can be represented by the following equation: If $s(t) = A\cos(2\pi f_c t)$ for binary 1 than $s(t) = A\cos(2\pi f_c t + \pi)$ for binary 0. In PSK modulation, non-return-to-zero (NRZ) signaling is used. The bandwidth requirement for PSK is, $\mathrm{BW} = 2\mathrm{Rb} = 2\mathrm{Bitrate}$. Compared with amplitude shift keying (ASK) and frequency

shift keying (FSK), the probability of error of PSK is less and SNR is higher. Moreover, BPSK is a power-efficient system but with lower bandwidth efficiency. The lower bandwidth efficiency property of the BPSK helps us to simulate the performance of the spatial SIC at each central frequency, since the frequency is one of the major parameters affecting the shape of beamforming produced by BF. By sweeping the frequency of the carrier wave, we explore the FD SIC performance when interfered with the side lobes or grating lobes caused by changing of the frequency. On the other side, by sweeping the steering angle of the BF, we investigate the interference, which is the side lobes or grating lobes from BF produced by changing the steering angle. After the BPSK simulation, we conduct a QPSK-based OFDM in different scenarios. QPSK is a digital modulation technique, which is bandwidth-efficient as each signal point represents two bits. Compared with simple BPSK modulation, QPSK utilized phase encoding in the complex plan with phase shifts of multiples of 90 degrees i.e., $\pi/2$, instead of a phase shift of 180 degrees, as allowed in BPSK. It leads to more challenges with inter-carrier interference (ICI) and ISI in the situation of very long delay spreads, posing the possibility that the channel length exceeds [40]. There are two sources of ICI, which are introduced by insufficient CP and channels variations. They are different and the existing literature analyzes them separately and takes different methods to mitigate them.

For a QPSK system, the phase or amplitude noise can lead to a degradation in the received signal's SNR, then cause inefficient system power. Techniques like phase-sensitive amplification or signal processing with coherent summation with higher-order harmonic are designed to achieve a more concentrated "phase squeezing" [41]. In our proposed spatial beamformed SIC, there is a trade-off between the steering angle range and the performance of QPSK. The available bandwidth is limited by the design of the transducer as well as the range of steering angle. From (12), we know the relationship between steering angle and wavelength, which is one of the two sides of frequency and array spacing, which can be tuned by the design of a transducer. In the case of a steering angle range, the spatial factor $M_S(f)$ generates a new distribution in the frequency domain. However, unlike the methods mentioned in advance, $M_S(f)$ is usually an asymmetric mask, which mitigates the phase noise but imbalanced high-low frequency compared with the central frequency of the transducer. The spatial factor $M_S(f)$ is expressed as the combination of a low pass filter $M_L(f)$ and a high pass filter $M_H(f)$,

$$M_S(f) = M_L(f + f_0) \times M_H(f - f_0). \tag{13}$$

The balanced condition only appear when $M_S(f)$ is equal to or slightly higher than $M_H(f)$ and $M_L(f)$. Under this condition, the frequency response results from the beamforming in the space matches OFDM the most, leading to the best performance. On the contrary, if any of $M_S(f)$, $M_H(f)$ or $M_L(f)$ is lower than two others, the frequency response results from the beamforming in the space works similarly to a band-stop filter. The band-stop filter stops the signal at or nearby the central frequency of the PAT. Under this situation, due to influence in the blocked bands, the increase of bandwidth is of no benefit to the performance of FD communication.

IV. Performance Evaluation

The performance of our spatial SIC system has been evaluated from both physical-layer channel estimation and experiments. In Sec. IV-A, the BER and signal-to-interference ratio (SIR) are simulated in different steering angle scenarios. Besides, the packet delivery ratio (PDR) versus channel SNR are deployed in different steering angles as well as different BPSK center frequencies. To consider real-world challenges, the spreading of sound in shallow sea water, which is exclusively cylindrical, is considered. In Sec. IV-B, a UWA experiment is conducted on the Littoral ocean observatory network (LOON) testbed hosted at the NATO science and technology organization centre for maritime research and experimentation (CMRE) [42] in June 2021. We show SI, intended signal, and emulated spatial SIC results here. Moreover, MUSIC DoA estimation is deployed on the FPGA board for estimating the feasibility of the spatial SIC working in real-time on the FPGA-based mode. The performances of traditional PSK and PSK-OFDM demonstrate that our proposed solution can explain the phenomenon introduced by the beamforming when doing SIC from idea simulation to real-world underwater channel when compromised by the strong multipath effect, Doppler effect, and imperfect frequency response of equipment and the experimental environment.

A. Simulation Results

The spatial SIC scheme performance with an underwater channel model is simulated through Simulink. We individually modulated randomly generated bits with BPSK and QPSK-OFDM. Noted that the frequency response of the transducer and hydrophones is ignored, we focus on the spatial effects of the PAT and the underwater channel, which are shown in Fig 7. Sound intensity attenuated underwater results in the influence of chemical components [43]. The signal source for the underwater acoustic channel is binary random bits at a center frequency. Then we convert unipolar to bipolar in the databits. Further, the bipolar bits are modulated with the intended modulation method. In the channel block's model, an additive white Gaussian noise (AWGN) channel with adjustable SNR is considered. The UWA channel absorption to build the absorption function block is taken from [43]. In order to mimic the stable seawater environment, we set the parameters as Table II.

Our Simulink simulation blocks arrangement is shown in Fig. 8, the random integer generator block generates uniformly distributed random binary integers, either 0 or 1, to encode BSPK in the desired carrier wave. A spatial SIC attenuation block on the SI path is designed as a gain of the direct SI signal. The amplitude corresponding to the steering angle is shown in Fig. 9. We calculate the values of the absorption coefficient for different frequencies and the variances needed to generate our wave noise. In Simulink, there are not blocks capable of accurately representing the colored Gaussian noise paired with the absorption coefficient used in our research. For the purpose of remedying this problem, we used s-functions

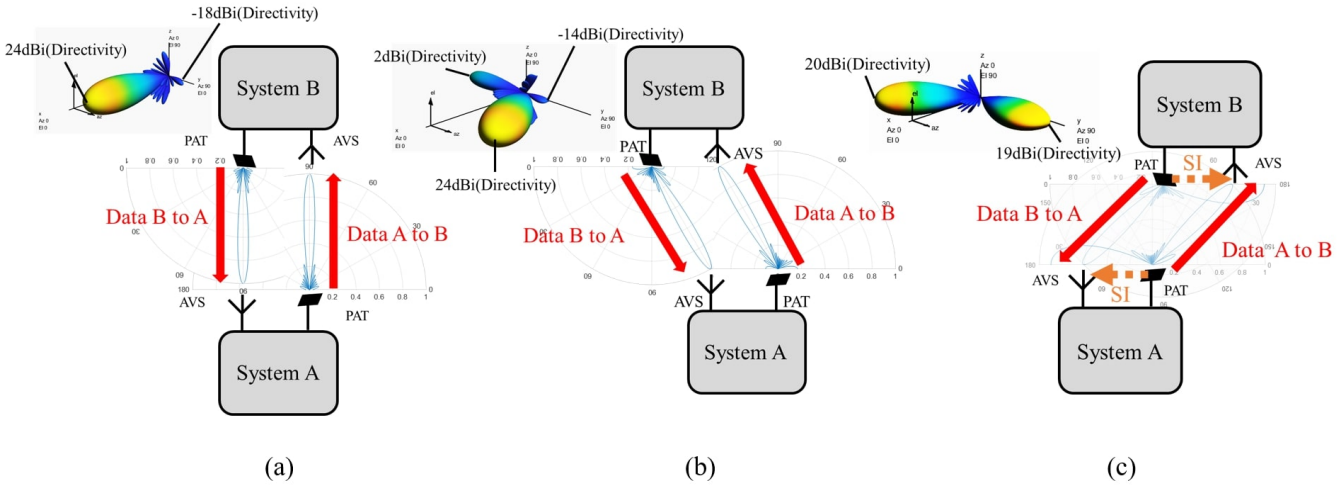

Fig. 7. (a) FD spatial SIC solution while the relative location of system A and system B is fixed in the front; (b) Relative location is changing in an angle region (within -30 to 40 degrees), take 30 degrees, for instance, the grating lobe appears on the opposite of the mainlobe; and (c) When relative location is below -40 degree, take -45 degree for instances, the grating lobe appears on the angle aiming to the AVS of the same system, which becomes the direct SI.

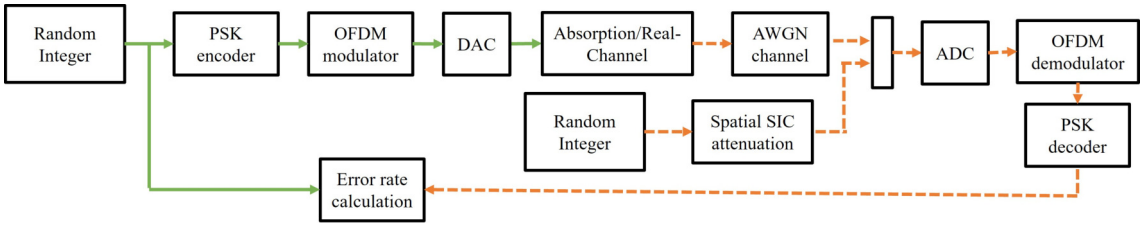

Fig. 8. Simulink UWA FD SIC simulation blocks for PSK OFDM signals. In simulations, an absorption block is considered; in the emulation using the real channel, the channel block featured by the real channel impulse response is considered (green solid line: intended signal; orange dash line: interfered signal).

to program and incorporated them into our simulation model. To ensure the strength of signal transmission and sensitivity of signal reception, we have chosen the frequency within the working range of the PAT from 80 to 120 kHz. We consider signal attenuations are boric acid and magnesium sulfate [43]. Numerous factors and properties of sea water, such as acoustic frequency, pressure, acidity, temperature, and salinity, play a role in the characterization of the absorption coefficient.

The acoustic transmission can either be cylindrical or spherical. In shallow water, the spreading is exclusively cylindrical [44] and the transmission loss (TL), in dB, is given by $\mathrm{TL} = 10\log(\mathrm{r}) + 10^{-3}\alpha \mathrm{r}$, where r represents the distance between the Tx and the Rx in km, and α is the absorption coefficient in dB/km. Our expected range of transmission is 10 m. By referring absorption model in [45–47], the absorption coefficient, in dB/km, is

$$\alpha = \left(\frac{A_1 P_1 f_1}{f^2 + {f_1}^2} + \frac{A_2 P_2 f_2}{f^2 + {f_2}^2} + A_3 P_3 \right) f^2, \qquad (14)$$

where f represents the frequency, in kHz, of the sound wave being transmitted over the channel.$A_1$is the boric acid component in sea water and is given by,

$$A_1 = \frac{8.68}{c} 10^{(0.78pH-5)}, \qquad (15)$$

where pH is the pH of sea water and c is the sound speed; T is the temperature of the water (in degrees Celsius), P_1 is the depth pressure of boric acid in sea water. Its normalized value for shallow waters is 1 Pa.

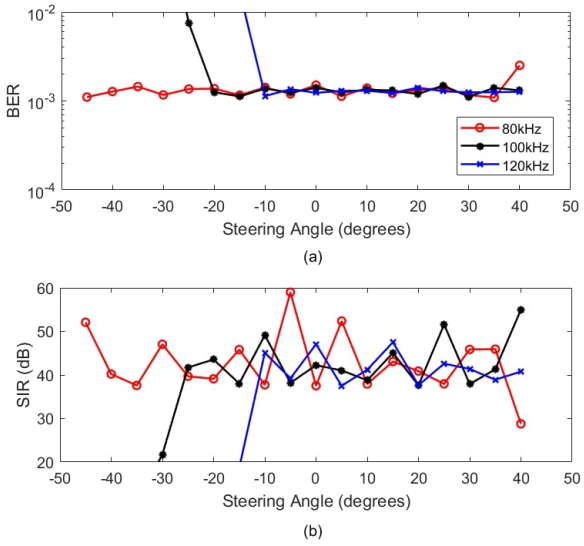

Fig. 9. Simulation results of (a) BER; and (b) SIR versus steering angle with 12-element PAT, in which the ratio of d over λ is 0.57 at center frequency 100 kHz. 80 kHz and 120 kHz are lower and upper bound in the frequency response of the PAT.

Boric acid relaxation frequency is denoted by f_1 (in kHz) in (14), and is given by,

$$f_1 = 2.8\left(\frac{S_a}{35}\right)^{\frac{1}{2}} 10^{(4-\frac{1245}{273+T})}. \qquad (16)$$

Here, S_a is the salinity in mg/l, magnesium sulfate relaxation

TABLE II
UNDERWATER CHANNEL CHARACTERISTICS AND PARAMETERS.

PAT Frequency [kHz]	**Depth** [m]	**Temp.** [$^\circ C$]	**Salinity** [ppt]	**pH**
100	10	25.86	36.88	7.3

frequency f_2 (in kHz) is given by,

$$f_2 = \frac{8.17}{1 + 0.0018(S - 35)} 10^{(8 - \frac{1990}{273+T})}. \tag{17}$$

A_2, the magnesium sulfate component is expressed as,

$$A_2 = 21.44\Big(\frac{S_a}{c}\Big)(1 + 0.025T). \tag{18}$$

P_2 (in Pa) is the depth pressure for magnesium sulfate,

$$P_2 = 1 - 1.37 \times 10^{-4} z + 6.2 \times 10^{-9} z^2, \tag{19}$$

where z is the depth of the water. Pure water component in the sea A_3 is given by,

$$\begin{aligned} A_3 = {} & 3.964 \times 10^{-4} - 1.146 \times 10^{-5} T \\ & + 1.45 \times 10^{-7} T^2 - 6.5 \times 10^{-10} T^3. \end{aligned} \tag{20}$$

Pure water depth pressure is P_3 (in Pa) and is given by,

$$P_3 = 1 - 3.83 \times 10^{-5} z + 4.9 \times 10^{-10} z^2. \tag{21}$$

The AWGN block adds white Gaussian noise to the input signal. The white noise variance can be adjusted using the variance block, which computes the unbiased variance of the noise. On the other hand, with the randomly generated BPSK signal as the interference, we ignore the absorption since it's geometrically closed to the receiver.

The BF is designed to be able to let PAT aim at any angle while the relative location of system A and system B is changing. However, this mechanism is not flawless. Take BPSK at 100 kHz carrier wave as an example, while aiming forward (0° on the Fig. 7(a)), the sidelobes are suppressed nicely. When aiming 30° different from forward (30° in Fig. 7(b)), the sidelobes are still constrained. The threshold happens around -40°. While aiming to -45° (Fig. 7(c)), the grating lobe on 0° is significantly increased. In this situation, the spatial SIC is invalid. Here, we make a draw conclusion. If the steering angle exceeds the threshold angle (acquired by (12)), the issue can be solved from (i) Still installing an analog SIC circuit as an enhancement or (ii) Rotating the underwater robot/vehicle body or (iii) Enabling the mechanical structure to change the angle of PAT substrate angle.

Fig. 9(a) shows the BER versus steering angle of the transmitter. We can observe for BPSK at 80 kHz signal, the spatial SI is canceled nicely within -40° to 40°. The BER is controlled within 1.09×10^{-3} to 2.51×10^{-3}. For the BPSK at 100 kHz carrier wave, the BER performs well while the steering angle is above -25°. Due to the grating lobe, the BER rises quickly to 1.87×10^{-2} when steering to -35°. For 120 kHz carrier wave, the steering angle becomes more constrained. The BER rises to 2.5×10^{-2} when steering to -20°. The SIR, is the quotient between the average received modulated carrier power and the average received co-channel interference power i.e. crosstalk, from other transmitters than the useful signal. To compute SIR, we must distinguish the power of the desired signal, S, from the power of the interfering signal(s), I. The SIR is thus: $SIR = S/I$. When expressed in dB, the SIR is: $SIR(dB) = S(dBm) - I(dBm)$. SIR in Fig. 9(b) acquired from Fig. 8 shows for lower frequency, the angle is not restricted from -40° to 40° in space. However, for a higher frequency, the aperture becomes smaller. This is a trade-off between space and frequency while choosing spatial SIC as the first stage SIC method. For broadband applications, the aperture is limited. Otherwise, for the wide view in space, the frequency bandwidth is limited. Even so, our proposed method can still achieve the bandwidth in frequency better than general UWA FD SIC in a limited aperture.

Figs. 10 and 11 show the simulation results of BPSK-based OFDM in AWGN channel SNR versus PDR. The x-axis marked as HD Link SNR is the single direction of the channel SNR in FD communication, the performance of PDR on y-axis is evaluated under the condition of single direction by considering the SI from the same side of the receiver in the FD mode. The PDR is the ratio of packets successfully received to the total sent. In our case, it help us check, as the carrier frequency changed, how the SIR influenced by beamforming pattern result in delivery fail on the receiver side. Packets are the basic units of communication over the FD communication link from randomly generated PSK encoded signals. We simulated a sequence of 5 OFDM streams, each OFDM stream contains 20 OFDM packets, and each OFDM packet is 10-Byte long. As the SNR rises, the PDR can not converge to 1 for higher steering frequencies at negative angles due to the weak performance of the spatial SIC. Fig. 10(a) shows for low-frequency carrier wave, the performance of spatial SIC works well as steering angle sweep to -45°. From Fig. 10(b), we found when to steer at -35°, which serves as the critical angle. The ability of SIC is 10.2 dB start unable to let Link PDR converge to 1. In this way, the following digital cannot cancel the residual SI as well. In Fig. 10(c) the aperture is more restricted to -20°. Comparing Fig. 11(b) with Fig. 11(a), when the PAT is aiming at a more negative angle, more high-frequency signals SIC could not work. It is noteworthy that in Fig. 11(c), the SIR raised again while PAT is steering at -40°. The reason is when steering to such a negative angle, the grating lobe already went past. This served as a band-stop filter in space. The stopped bandwidth is equal to the beamwidth of the grating lobe. All the results according to Figs. 10 and 11 valid the influence of SIR caused by the beamforming, while changing the frequency or the steering angle, the shape of the beamforming pattern is also be adjusted and can be checked with the relationship between Fig 9.

In the QPSK-based OFDM signal simulation shown in Fig. 8, the QPSK encoder is designed to encode the randomly generated signals into the narrow band or well-defined bandwidth between the lowest frequency and highest frequency. For example, we take the parameter of the central frequency 100 kHz of the PAT described in Sec. III-A. We also simulate the performance of 80 kHz and 120 kHz. Besides, we take advantage of the frequency bandwidth distribution of OFDM, and we simulate the QPSK-OFDM in three different bandwidths, including lowest frequency to central frequency and central frequency to highest frequency. The simulation results of QPSK-OFDM corresponding to different steering

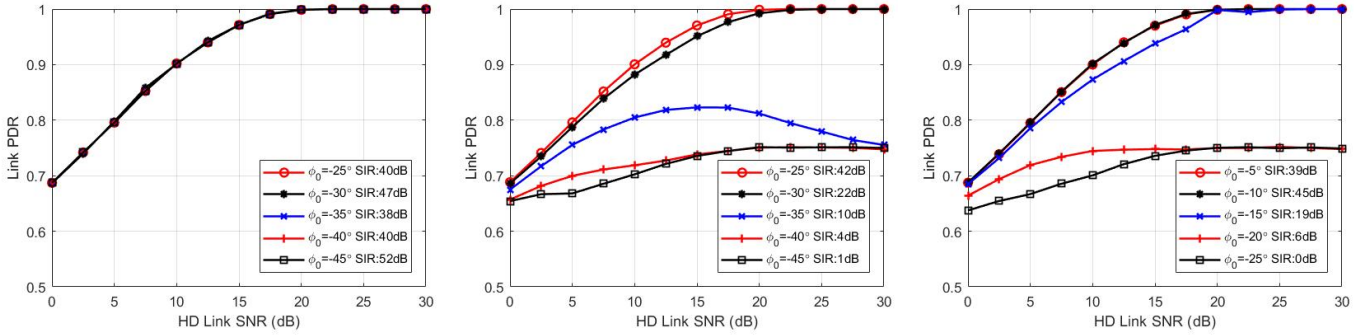

(a) (b) (c)

Fig. 10. Simulation results of full-duplex BPSK AWGN channel link SNR versus PDR at center frequency of (a) 80 kHz; (b) 100 kHz; and (c) 120 kHz. Note that in the 80 kHz condition, all angles are keeping good SIR, which results in good link PDR in (a).

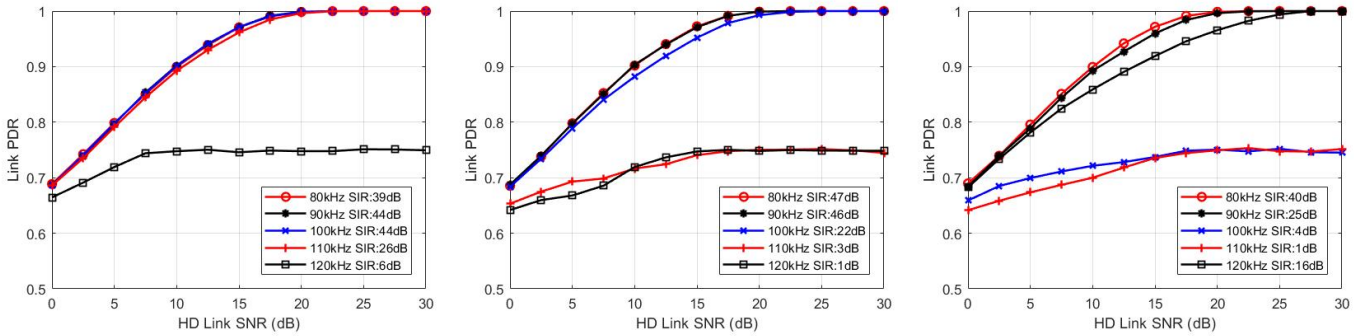

(a) (b) (c)

Fig. 11. Simulation results of full-duplex BPSK AWGN channel link SNR versus PDR with steering angle of (a) $-20°$; (b) $-30°$; and (c) $-40°$.

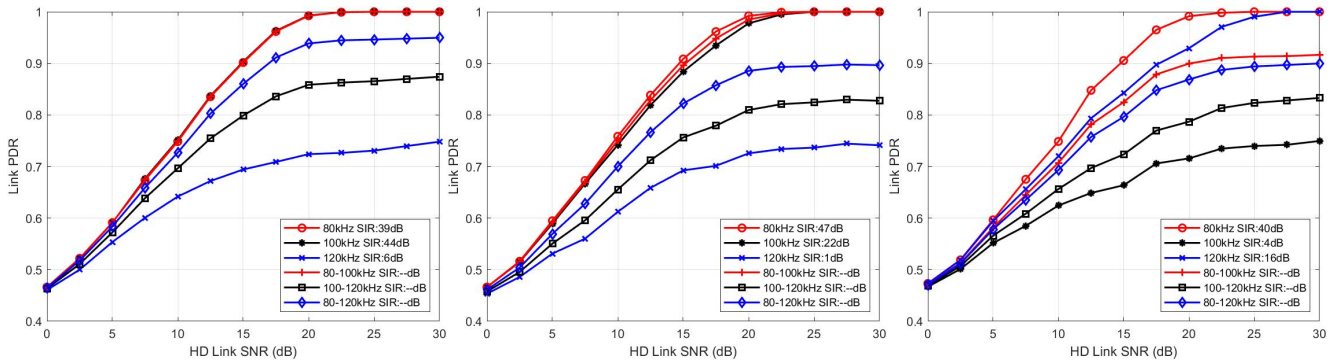

(a) (b) (c)

Fig. 12. Simulation results of full-duplex QPSK-based OFDM AWGN channel link SNR versus PDR (a) Steering angle:$-20°$; (b) Steering angle:$-30°$; and (c) Steering angle:$-40°$.

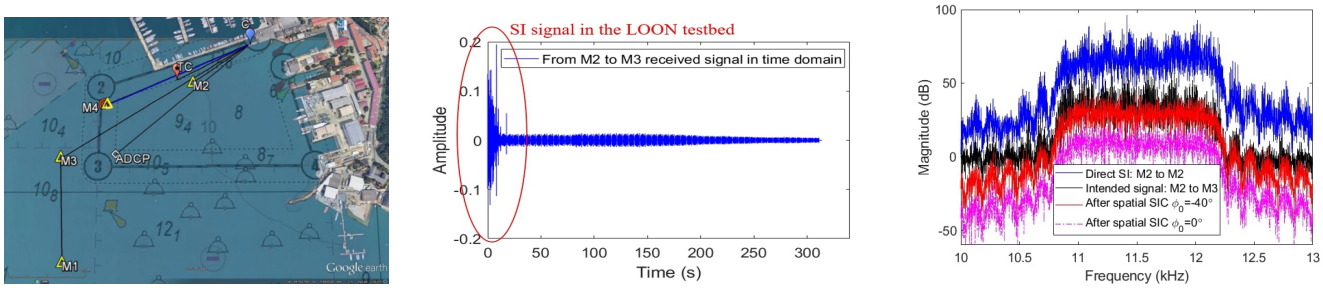

(a) (b) (c)

Fig. 13. (a) Geographic configuration of the LOON testbed, in the Gulf of La Spezia, Italy; (b) Received signal from M2 to M3 in the LOON testbed including SI signal within $0-25$ s; and (c) The frequency spectrum of LOON M2 to M2, M2 to M3 OFDM experiment signal and emulation results of spatial SIC steering on $-40°$ and $0°$.

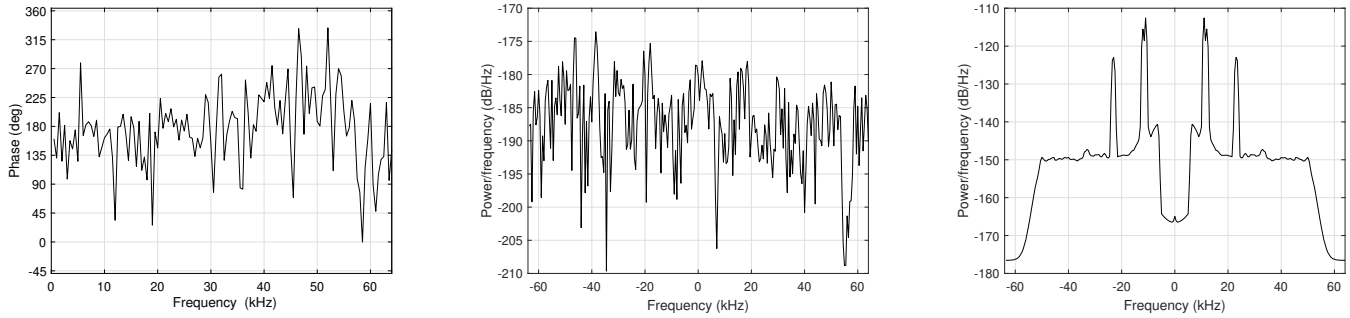

(a) (b) (c)

Fig. 14. Channel state information collected by LOON testbed in June, 2021: (a) Phase of the channel response in the at-sea experiment; (b) Power spectrum of the channel response in the at-sea experiment; and (c) Power spectrum of the received signals in the at-sea experiment.

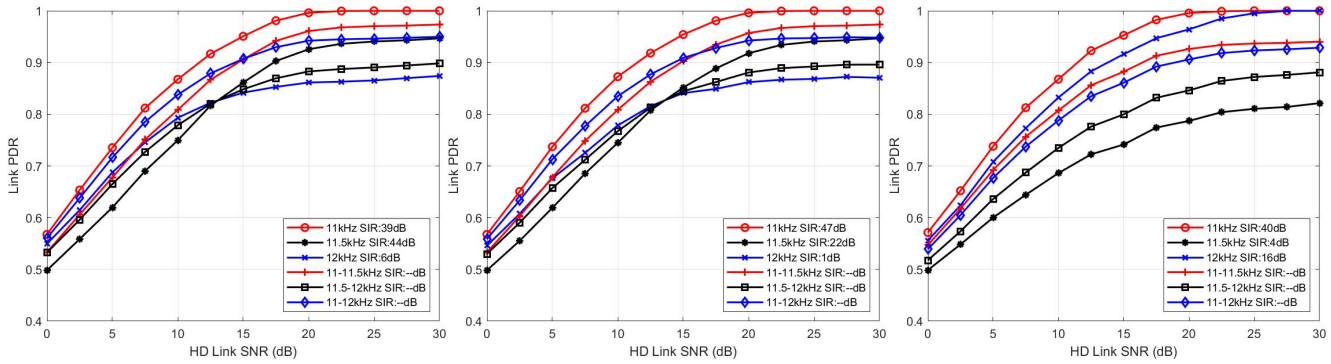

(a) (b) (c)

Fig. 15. Emulation results of full-duplex QPSK-based OFDM on real channel acquired from LOON testbed link SNR versus PDR (a) Steering angle:$-20°$; (b) Steering angle:$-30°$; and (c) Steering angle:$-40°$.

(a) (b) (c)

Fig. 16. (a) Photo of an ARM-based FPGA board called PYNQ-Z2; (b) Measured DC voltage, current and power at USB port show the stable low power consuming and low voltage requirement are friendly for portable devices battery; and (c) MUSIC DoA estimation executed on FPGA PYNQ-Z2, in which the signal is designed from $14°$ on the horizontal plane.

angles are shown in Figs. 12 with different scenarios of $M_S(f)$. First, we observe the 80 kHz, 100 kHz and 120 kHz narrow band modulated QPSK signals steering at angle $-20°$, $-30°$ and $-40°$ have the same trend compared with Fig. 11. The BER of QPSK-OFDM is higher than BPSK, leading to PDR lower than BPSK while utilizing spatial SIC. For convenience of reference, we define 80–100 kHz as BW1, 100–120 kHz as BW2 and 80–120 kHz as BW3. $M_S(f)$ balanced condition as Cond1, unbalanced due to small M_H as Cond2 and unbalanced due to small M_L as Cond3. In Figs. 12(a), the steering angle is equal to $-20°$, BW1 is Cond1 results in good performance. BW2 is Cond2 results in compromised performance. BW3 is also Cond2 but has a greater portion of balanced bandwidth, leading to compromised but better than BW2 result. In Figs. 12(b), the steering angle is equal to $-30°$, BW1 is Cond1 results in good performance. BW2 is Cond2 results in compromised performance. BW3 is also Cond2 but has a greater portion of balanced bandwidth, which leads to compromised but better than BW2 result. In Figs. 12(c), the steering angle is equal to $-40°$, BW1 is Cond2 results in compromised performance. BW2 is Cond3 results in compromised performance. BW3 has a frequency response the same as the band-stop filter and performs slightly better than BW1 or BW2.

To better analyze the trade-off between frequency bandwidth and space spectrum, we observe the QPSK signals in the Figs. 12(a), where we have bandwidth BW1, BW2, and BW3 at steering angle $-20°$. For BW1, $M_S(90\text{ kHz})$, $M_L(80\text{ kHz})$, and $M_H(100\text{ kHz})$ are well balanced, which leads to a good performance for packet delivery. For BW2, $M_S(110\text{ kHz})$, $M_L(100\text{ kHz})$, and $M_H(120\text{ kHz})$ are not balanced, $M_H(120\text{ kHz})$ is lower than two others leads to a compromised packet delivery. Finally, for BW3, $M_S(100\text{ kHz})$, $M_L(80\text{ kHz})$, and $M_H(120\text{ kHz})$ are not balanced, $M_H(120\text{ kHz})$ is lower than two others but $M_S(100\text{ kHz})$ and $M_L(80\text{ kHz})$ are partially balanced, hence the packet delivery is better than for BW2. As we compare BW3 bandwidth QPSK in Figs. 12(a), (b), and (c), $M_{-20}(100\text{ kHz})$ is better balanced than $M_{-30}(100\text{ kHz})$ and $M_{-40}(100\text{ kHz})$. Therefore, SIC is having a better performance when steering at $-20°$.

B. Experiment and Emulation Results

To verify the performance of the proposed method with a real testbed, a bunch of UWA signal experiments are conducted at LOON testbed [42] to collect the required acoustic data, which are then used in MATLAB emulations to validate the proposal, since the LOON testbed cannot process package data online. The CMRE LOON testbed, a permanent infrastructure, is deployed in the gulf of La Spezia, Italy. This testbed is composed of 4 mounted tripods with acoustic communication transducers, i.e., M1, M2, M3, and M4 in Fig. 13(a). We take nodes M2 and M3 for SI testing. Fig. 13(b) shows the SI in the received signal. We consider signal M2 to M2 as the direct path SI. The distance between M2 and M3 is around 460 m and they are installed at a depth of about 10 m. In Figs. 14(a) and (b), the phase response and the the power spectrum of the at-sea channel during the experiments are shown, respectively. The power spectrum of the received signals is shown in Figs. 14(c), where the carrier frequency is 11.5 kHz. The DAC sampling rate is 48 kHz. The ADC sampling rate is 128 kHz. The OFDM modulated signal length around $5:19$ at center frequency 11.5 kHz with bandwidth 9600 Hz has been tested. Fig. 13(c) shows the frequency spectrum of SI, intended signal, spatial SIC on steering angle $-40°$ and $0°$. The power spectrum shows the ability of spatial SIC, it is possible that SI to be canceled to the noise floor level by further applying digital SIC according to [6]. After spreading such distance, the SI signal is 27 dB stronger than the intended signal. In order to emulate the spatial SIC in the LOON testbed, we design a PAT, which follows the ratio of d over λ in Sec. III-A, which is 0.57 but now at the center frequency 11.5 kHz. The SIR on steering angle $-40°$ and $0°$ at center frequency are respectively 22 dB and 41 dB. The PSK OFDM emulation is shown in Fig. 15. We projected previous results and the corresponding beamforming shape into the real channel, whose frequency band is from 11 kHz to 12 kHz, then we put the real channel into emulation with the property of Figs. 14. The emulation shows the spatial SIC can work in the real channel, followed by the bandwidth and condition we presented in Sec. IV-A. However, the performance can be compromised by the more complex real channel scenario, including the frequency response of the transducers, severe multipath and Doppler effect. In the simulation of AWGN and absorption model channel shown in Fig. 12, it is easier to observe the influence on Link PDR in different single frequency or frequency interval. On the other hand, the complexity of real channel lead to cross-points in Fig. 15 and become finer division of performance in Link PDR as comparing different SNR. Although generally, the PDR becomes better but fewer bandwidths can converge PDR to 1. In order to estimate the feasibility of the spatial SIC working in real-time on the FPGA-based model, we adopt the DoA estimation algorithms MUSIC on FPGA PYNQ-Z2 (Fig. 16(a)) by Xilinx, Inc. The dimension of PYNQ-Z2 is $13.5\times8.5\times2$ (cm^3), which is suitable for mounting in the AUV. Fig. 16(b) shows the measured USB DC voltage and current shows it consumes only about 2 W. The location information signal is designed on $14°$ on the (x–y plane) and is received by a 12-element sensor array. The run-time is 1.22×10^{-4} s, which is promising for real-time application since MUSIC is the most complex method within acoustic intensity, BB and CB methods. The DoA result from PYNQ-Z2 is shown in Fig. 16(c).

V. Conclusion and Future Work

We presented a novel underwater acoustic communications SIC method to double the underwater acoustic spectral efficiency and allow simultaneous transmission and reception in FD modality. This SIC in space domain is designed to be an alternative to the traditional analog SIC in FD communication. To realize the spatial SIC, the proposed technique utilizes underwater AVSs and a PAT as well as an adaptive protocol. The protocol helps FD UWA communication establish a reliable communication with spatial SIC on both side of the link. By updating DOA from information acquired with AVS, the BF

helps PAT adjust steering angle to aim at the other side of the link, therefore transmits intensive signals with mainlobe in beamforming. We presented the results via simulations, experiments, and emulations with traditional underwater model and real underrate channel, PSK and PSK-based OFDM are deployed for modulation. It was confirmed that the aperture in space becomes smaller for higher frequencies. When the signal is modulated using a wider bandwidth, including higher frequency signals, a trade-off between the apertures of spatial SIC should be considered; we demonstrated that feasibility and effectiveness of FD SIC in different conditions including different modulations, frequency bandwidths, relative angles in the space. Although we propose the possibility of extending the FD system to a diverse multi-user network with different modulation methods, algorithms for optimized protocols and modulations will be the scope of future work. As the UWA FD SIC is equipped with a compact FPGA board, not only the proposed method can work efficiently in terms of energy, but also more functions can be developed and experimentally tested. The benefit of fast machine learning (ML) classification on FPGA is also a promising path on the trained data of FD SIC, as well as novel DOA estimation techniques to further aid spacial SIC in complex scenarios.

VI. Acknowledgements

The authors thank Dr. Roberto Petroccia and the NATO Centre for Maritime Research and Experimentation (CMRE) for the help with data and experiments.

References

[1] Y.-T. Hsieh, M. Rahmati, and D. Pompili, "FD-UWA: Full-duplex underwater acoustic comms via self-interference cancellation in space," in *Proc. IEEE MASS*, 2020.

[2] J. Zhou *et al.*, "Integrated full duplex radios," *IEEE Commun. Mag.*, vol. 55, no. 4, pp. 142–151, 2017.

[3] G. Qiao, S. Gan, S. Liu, and Q. Song, "Self-interference channel estimation algorithm based on maximum-likelihood estimator in in-band full-duplex underwater acoustic communication system," *IEEE Access*, vol. 6, pp. 62324–62334, 2018.

[4] A. El Sayed *et al.*, "A full-duplex receiver with 80 MHz bandwidth self-interference cancellation circuit using baseband Hilbert transform equalization," in *Proc. IEEE RFIC*, 2017.

[5] M. B. Dastjerdi, N. Reiskarimian, T. Chen, G. Zussman, and H. Krishnaswamy, "Full duplex circulator-receiver phased array employing self-interference cancellation via beamforming," in *Proc. IEEE RFIC*, 2018.

[6] T. Chen, M. Baraani Dastjerdi, J. Zhou, H. Krishnaswamy, and G. Zussman, "Wideband full-duplex wireless via frequency-domain equalization: Design and experimentation," in *Proc. ACM MobiCom*, 2019.

[7] L. Shen, B. Henson, Y. Zakharov, and P. Mitchell, "Digital self-interference cancellation for full-duplex underwater acoustic systems," *IEEE Trans. Circuits Syst. II, Exp. Briefs*, vol. 67, no. 1, pp. 192–196, 2019.

[8] L. Jiang-Qiao *et al.*, "Autocorrelation based modulation recognition of PSK signals for OFDM in underwater acoustics communication," in *Proc. IBCAST*, 2018.

[9] M. Rahmati, Z. Qi, and D. Pompili, "Underwater adaptive video transmissions using MIMO-based software-defined acoustic modems," pp. 1–13, 2021.

[10] S. Zhao, T. Saluev, and D. L. Jones, "Underdetermined direction of arrival estimation using acoustic vector sensor," *Signal Process.*, vol. 100, pp. 160–168, 2014.

[11] M. Wajid, A. Kumar, and R. Bahl, "Direction-of-arrival estimation algorithms using single acoustic vector-sensor," in *Proc. IMPACT*, 2017.

[12] M. Rahmati and D. Pompili, "SSFB: Signal-space-frequency beamforming for underwater acoustic video transmission," in *Proc. IEEE MASS*, 2017.

[13] C. Wang, J. Yin, D. Huang, and A. Zielinski, "Experimental demonstration of differential OFDM underwater acoustic communication with acoustic vector sensor," *Appl. Acoust.*, vol. 91, pp. 1–5, 2015.

[14] T. Kim, K. Min, and S. Park, "Self-interference channel training for full-duplex massive MIMO systems," *Sensors*, vol. 21, no. 9, pp. 3250–3268, 2021.

[15] S. A. Hassani, K. Parashar, A. Bourdoux, B. van Liempd, and S. Pollin, "Doppler radar with in-band full duplex radios," in *Proc. IEEE INFOCOM*, 2019.

[16] T. Chen, M. B. Dastjerdi, H. Krishnaswamy, and G. Zussman, "Wideband full-duplex phased array with joint transmit and receive beamforming: Optimization and rate gains," in *Proc. ACM MobiHoc*, 2019.

[17] A. Mohammadi, M. Rahmati, and H. Malik, "Location-aware beamforming for MIMO-enabled UAV communications: An unknown input observer approach," *arXiv preprint arXiv:2111.10665*, 2021.

[18] L. Shen, B. Henson, Y. Zakharov, and P. D. Mitchell, "Adaptive nonlinear equalizer for full-duplex underwater acoustic systems," *IEEE Access*, 2020.

[19] L. Li, A. Song, L. J. Cimini, X.-G. Xia, and C.-C. Shen, "Interference cancellation in in-band full-duplex underwater acoustic systems," in *OCEANS 2015-MTS/IEEE Washington*. IEEE, 2015, pp. 1–6.

[20] Z. Guo *et al.*, "Self-interference characterization for in-band full duplex underwater acoustic communications," in *Proc. WUWNet*, 2019.

[21] Y. Kida *et al.*, "Performance analysis of passive time reversal communication technique for multipath interference in shallow sea acoustic channel," *Jpn. J. Appl. Phys.*, vol. 56, no. 7S1, pp. 07JG04–07JG12, 2017.

[22] G. Qiao, Y. Zhao, S. Liu, and N. Ahmed, "The effect of acoustic-shell coupling on near-end self-interference signal of in-band full-duplex underwater acoustic communication modem," in *Proc. IBCAST*, 2020.

[23] M. Towliat, Z. Guo, L. J. Cimini, X.-G. Xia, and A. Song, "Self-interference channel characterization in underwater acoustic in-band full-duplex communications using OFDM," in *Global Oceans 2020: Singapore – U.S. Gulf Coast*, 2020.

[24] D. V. Ha, V. D. Nguyen, and Q. K. Nguyen, "Modeling of Doppler power spectrum for underwater acoustic channels," *J. Commun. Netw.*, vol. 19, no. 3, pp. 270–281, 2017.

[25] Y. Zhang *et al.*, "Adaptive OFDMA with partial CSI for downlink underwater acoustic communications," *J. Commun. Netw.*, vol. 18, no. 3, pp. 387–396, 2016.

[26] Z. Qi, X. Zhao, and D. Pompili, "Range-extending optical transceiver structure for underwater vehicles and robotics," in *Proc. WUWNet*, 2019.

[27] Z. Qi, R. Petroccia, and D. Pompili, "ASVTuw: Adaptive scalable video transmission in underwater acoustic multicast networks," in *Proc. WUWNet*, 2022.

[28] K. Anjum, Z. Qi, and D. Pompili, "Deep joint source-channel coding for underwater image transmission," in *Proc. WUWNet*, 2022.

[29] Z. Qi and D. Pompili, "UW-CTSM: Circular time shift modulation for underwater acoustic communications," in *Proc. WONS*, 2022.

[30] Z. Qi and D. Pompili, "Spatial modulation-based orthogonal signal division multiplexing for underwater ACOMMS," in *Proc. UComms*, 2022.

[31] Y.-T. Hsieh, Z. Qi, and D. Pompili, "ML-based joint doppler tracking and compensation in underwater acoustic communications," in *Proc. WUWNet*, 2022.

[32] H. Guo, A. Abdi, A. Song, and M. Badiey, "Correlations in underwater acoustic particle velocity and pressure channels," in *Proc. CISS*, 2009.
[33] Y. Zou, Z. Liu, and C. Ritz, "Enhancing target speech based on nonlinear soft masking using a single acoustic vector sensor," *Appl. Sci.*, vol. 8, no. 9, pp. 1436–1452, 2018.
[34] B. Kumar, A. Kumar, and R. Bahl, "Comparative study of P-P and P-U based acoustic vector sensors for underwater application," in *Proc. OTO*, 2018.
[35] "RESON TC4013 hydrophone product information," http://www.teledynemarine.com/reson-tc4013, Last time accessed: May 2020.
[36] I. McCowan, "Microphone arrays: A tutorial," *Queensland University, Australia*, pp. 1–38, 2001.
[37] "Pmod GYRO: 3-axis digital gyroscope." [Online]. Available: https://digilent.com/shop/pmod-gyro-3-axis-digital-gyroscope/
[38] Y.-T. Hsieh, K. Anjum, S. Huang, I. Kulkarni, and D. Pompili, "Neural network design via voltage-based resistive processing unit and diode activation function - a new architecture," in *Proc. IEEE MWSCAS*, 2021.
[39] Hsieh *et al.*, "Hybrid analog-digital sensing approach for low-power real-time anomaly detection in drones," in *Proc. IEEE MASS*, 2021.
[40] S. Chen and C. Zhu, "ICI and ISI analysis and mitigation for OFDM systems with insufficient cyclic prefix in time-varying channels," *IEEE Trans. Consum. Electron.*, vol. 50, no. 1, pp. 78–83, 2004.
[41] A. Mohajerin-Ariaei *et al.*, "Phase noise mitigation of QPSK signal utilizing phase-locked multiplexing of signal harmonics and amplitude saturation," *Optics lett.*, vol. 40, no. 14, pp. 3328–3331, 2015.
[42] J. Alves, J. Potter, P. Guerrini, G. Zappa, and K. LePage, "The LOON in 2014: Test bed description," in *Proc. IEEE UComms*, 2014.
[43] M. C. Domingo, "Overview of channel models for underwater wireless communication networks," *Phys. Commun.*, vol. 1, no. 3, pp. 163–182, 2008.
[44] B. Zoh, "An underwater channel model and chirp slope keying modulation scheme performance," *University of New Orleans Theses and Dissertations*, 2010.
[45] R. Francois and G. Garrison, "Sound absorption based on ocean measurements: Part i: Pure water and magnesium sulfate contributions," *J. Acoust. Soc. Am.*, vol. 72, no. 3, pp. 896–907, 1982.
[46] Francois, RE and Garrison, GR, "Sound absorption based on ocean measurements. part ii: Boric acid contribution and equation for total absorption," *J. Acoust. Soc. Am.*, vol. 72, no. 6, pp. 1879–1890, 1982.
[47] M. A. Ainslie and J. G. McColm, "A simplified formula for viscous and chemical absorption in sea water," *J. Acoustical Soc. America*, vol. 103, no. 3, pp. 1671–1672, 1998.

Yung-Ting Hsieh (M'20) received the B.S. degree in Physics from National Chung Hsing University and M.S. degree in Acoustic Engineering from National Chiao Tung University in 2015 and 2017, respectively. In Summer'22, he worked at TE Connectivity as an Signal Integrity Electrical Engineering Intern. He is now working in the Cyber-Physical Systems Laboratory (CPS Lab) and pursuing a Ph.D. at Rutgers University in ECE. His research interests include wireless communication networks, engineering acoustics, and artificial intelligence (AI) hardware design.

Zhuoran Qi is a Ph.D. student in ECE at Rutgers University working with Prof. D. Pompili in the CPS Lab, which she joined in 2017. She received the B.E. degree from the University of Electronic Science and Technology of China in 2018 and M.S. degree from Rutgers in 2019. She is currently working on underwater acoustic and optical communications at the physical and network layer. She has received the Best Paper Award at the 2019 ACM International Conference on Underwater Networks and Systems (WUWNet).

Dario Pompili is a professor with the Dept. of ECE at Rutgers University. Since joining Rutgers in 2007, he has been the director of the Cyber-Physical Systems Laboratory (CPS Lab), which focuses on mobile edge computing, wireless communications and networking, acoustic communications, and sensor networks. He received his PhD in ECE from the Georgia Institute of Technology in 2007. He had previously received his 'Laurea' (combined BS and MS) and Doctorate degrees in Telecommunications and System Engineering from the U. of Rome "La Sapienza," Italy, in 2001 and 2004, respectively. He has received a number of awards in his career including the NSF CAREER'11, ONR Young Investigator Program'12, and DARPA Young Faculty'12 awards. In 2015, he was nominated Rutgers-NB Chancellor's Scholar. He served on many international conference Committees taking on various leading roles. He published about 200 refereed scholar publications, some of which received Best Paper Awards: with more than 14K citations, Dr. Pompili has an h-index of 47 and an i10-index of 129 (Google Scholar, Sept'22). He is a Fellow of the IEEE Communications Society (2020) and a Distinguished Member of the ACM (2019). He is currently serving as Associate Editor for IEEE Transactions on Mobile Computing (TMC) and Area Chair of IEEE INFOCOM.